

Stability limits for modes held in alternating trapping-expulsive potentials

Zhihuan Luo ¹, Yan Liu,¹ Yongyao Li ², Josep Batle ³, and Boris A. Malomed ^{4,5}

¹*Department of Applied Physics, South China Agricultural University, Guangzhou 510642, China*

²*School of Physics and Optoelectronic Engineering, Foshan University, Foshan 528000, China*

³*CRISP Centre de Recerca Independent de sa Pobla, C. Albéniz 12, 07420 sa Pobla, Balearic Islands, Spain*

⁴*Department of Physical Electronics, School of Electrical Engineering, Faculty of Engineering, and Center for Light-Matter Interaction, Tel Aviv University, Tel Aviv 69978, Israel*

⁵*Instituto de Alta Investigación, Universidad de Tarapacá, Casilla 7D, Arica, Chile*



(Received 22 March 2022; accepted 9 June 2022; published 1 July 2022)

We elaborate a scheme of trapping-expulsion management (TEM), in the form of the quadratic potential periodically switching between confinement and expulsion, as a means of stabilization of two-dimensional dynamical states against the backdrop of the critical collapse driven by the cubic self-attraction with strength g . The TEM scheme may be implemented, as spatially or temporally periodic modulations, in optics or BEC, respectively. The consideration is carried out by dint of numerical simulations and variational approximation (VA). In terms of the VA, the dynamics amounts to a nonlinear Ermakov equation, which, in turn, is tantamount to a linear Mathieu equation. Stability boundaries are found as functions of g and parameters of the periodic modulation of the trapping potential. Below the usual collapse threshold, which is known, in the numerical form, as $g < g_c^{(\text{num})} \approx 5.85$ (in the standard notation), the stability is limited by the onset of the parametric resonance. This stability limit, including the setup with the self-repulsive sign of the cubic term ($g < 0$), is accurately predicted by the VA. At $g > g_c^{(\text{num})}$, the collapse threshold is found with the help of full numerical simulations. The relative increase of g_c above $g_c^{(\text{num})}$ is $\approx 1.5\%$. It is a meaningful result, even if its size is small, because the collapse threshold is a universal constant which is difficult to change.

DOI: [10.1103/PhysRevE.106.014201](https://doi.org/10.1103/PhysRevE.106.014201)

I. INTRODUCTION

It is well known that two- and three-dimensional (2D and 3D) multidimensional solitons, maintained by the ubiquitous cubic self-attraction, are subject to severe instabilities, due to the fact that the same nonlinearity drives the critical and supercritical collapse, in the 2D and 3D cases, respectively [1–3]. The search for physically relevant settings which make it possible to stabilize self-trapped multidimensional states is a relevant problem, especially in the context of nonlinear optics and matter-wave patterns in Bose-Einstein condensates (BECs). Methods elaborated for this purpose include the use of quadratic interactions [4], higher-order defocusing nonlinearity, which may be represented by quintic terms, that occur in optics [5–11], and quartic ones, that account for the stabilization of *quantum droplets* by quantum fluctuations in binary BEC [12–14], spin-orbit coupling (SOC) acting on binary condensates [15–18], etc. [19,20], see reviews [21–26]. Experimentally, soon after the theoretical prediction of quantum droplets, they have been created in BEC with local [27–31] and nonlocal [32–35] interactions.

Straightforward means for the stabilization of 2D self-attractive fields with zero vorticity [i.e., fundamental states (FSs)] and vorticity $S = 1$ against the critical collapse is provided by the harmonic-oscillator (HO) trapping potential [36–43]. In particular, it has been found that the 2D collapse instability of all FS modes is completely removed by the HO potential, while the vortex modes remain unstable against

spontaneous splitting, only the ones with $S = 1$ and the norm falling below a certain threshold value being stabilized by the trapping potential. In addition to that, in an interval of values of the norm above the threshold there are stable dynamical states, in the form of vortices with $S = 1$ which periodically split in two fragments and recombine back, keeping the angular momentum.

On the other hand, expulsive quadratic (*anti-HO*) potentials also appear in a variety of physically relevant setups [44–53]. In guided-wave optics, expulsive potentials occur in antiwaveguiding systems, which are used to design various data-processing photonic schemes [54–57]. The latter application makes it relevant to consider the propagation of optical solitons through a waveguide built of alternating trapping and expulsive segments [58]. A similar setting is possible in BEC, with the external potential periodically [75] or temporarily [59,60] switching between the HO and anti-HO forms. It may be realized experimentally, using the usual optical trapping setup for BEC [61,62], pumped by modulated light, which periodically switches between red- and blue-detuned frequencies. Search for stable solitons existing under the joint action of the cubic self-attractive nonlinearity and periodically alternating trapping-expulsive potential places such settings in the class of systems which maintain solitons by means of various *management* techniques [63], a commonly known example being *dispersion management* of temporal solitons in optical fibers [64].

However, previous works considered the interplay of the self-focusing and periodically flipping HO–anti-HO potential only in 1D geometry. The objective of the present work is to develop this analysis for 2D solitons. It is a challenging problem because of the possibility of the critical collapse (blowup) in such a case. This circumstance links the present problem to the setting based on the *nonlinearity management* for 2D solitons in free space (in the absence of the trapping potential), which was originally introduced in optics, considering the propagation of $(2 + 1)$ D spatial solitons in bulk waveguides built as alternation of layers with self-focusing and defocusing Kerr nonlinearity [65]. Later it was extended for BEC in the quasi-2D geometry, with the sign of the contact nonlinearity periodically switching between attraction and repulsion under the action of the Feshbach resonance controlled by a periodically varying magnetic field [66–68].

In the case of the critical collapse, modelled by the 2D nonlinear Schrödinger equation (alias the Gross-Pitaevskii equation (GPE), in terms of the mean-field description of BEC [69]), a crucially important role is played by Townes solitons (TSs) [70], which realize the separatrix between decaying and collapsing solutions of the GPE in 2D. As any separatrix solution [71,72], the TSs are unstable against small perturbations. In the free space, the TS family is degenerate in the sense that all solitons belonging to it have a single value of the norm, N_{TS} . This value represents a threshold necessary for the onset of the collapse, as, at the late stage of the blowup, the collapsing mode becomes very narrow, hence the collapse ends up as in the nearly free space, even if an external potential is present. The system with the fully unstable TS family has no ground state (it is replaced by the collapsing one). In fact, the stabilization of the TSs by the trapping potential [36,38,41] or SOC [15,18] is underlain by the fact that the potential or SOC lifts the degeneracy, making it possible to create FS modes with $N < N_{\text{TS}}$, which are stable because the collapse does not take place in this case. However, such results did not demonstrate a possibility to stabilize states with $N > N_{\text{TS}}$. An essential result of the present work is that the application of the “trapping-expulsive management” (TEM) makes it possible to construct stable FS modes, in an oscillatory form, whose norm exceeds N_{TS} by a small but meaningful margin, $\approx 1.5\%$, while usually N_{TS} is a universal constant, which cannot be changed. Another major objective of the work is to identify robustness boundaries of the FS modes under the action of the TEM at $N < N_{\text{TS}}$ against the action of a different potentially destabilizing factor—the collapse but the parametric resonance (PR), which may occur when an internal mode of the FS trapped in the potential resonates with the TEM frequency.

The rest of this paper is structured as follows. The model is introduced in Sec. II. In that section, physical parameters for the realization of the model in BEC and optics are evaluated, too. The variational approximation (VA), which provides a relevant method to predict the stability of the FSs in the present model, is also elaborated in Sec. II. The VA replaces the GPE by a second-order nonlinear ODE (ordinary differential equation) of the *Ermakov’s type* (see details below). The latter equation is simulated numerically, but the onset of the instability, caused by the PR, is correctly predicted in an analytical form, as the Ermakov equation is tantamount to the

linear Mathieu equation. Results of the systematic numerical investigation, which demonstrate stability boundaries of the FSs against the critical collapse and PR alike, are summarized in Sec. III. In particular, the VA predicts the PR-instability boundary very accurately, including the system with the self-repulsive nonlinearity. The paper is concluded by Sec. IV.

II. THE MODEL AND VARIATIONAL APPROXIMATION

We adopt the single-component GPE, written in the scaled 2D form for the mean-field BEC wave function, ψ :

$$i \frac{\partial \psi}{\partial t} = -\frac{1}{2} \nabla^2 \psi - g |\psi|^2 \psi + \frac{1}{2} \kappa(t) r^2 \psi, \quad (1)$$

where $g > 0$ is the constant coefficient of the cubic self-attraction and r is the radial coordinate. TEM is introduced by making the strength of the quadratic potential a function of time, which includes dc (constant) and ac (variable) components, periodically flipping between positive and negative values:

$$\kappa(t) = \kappa_{\text{dc}} + \kappa_{\text{ac}} \cos(\omega t). \quad (2)$$

The case of basic interest is

$$\kappa_{\text{ac}} > \kappa_{\text{dc}} > 0, \quad (3)$$

as this condition maintains the sign-changing structure of function (2). The case of

$$0 < \kappa_{\text{ac}} < \kappa_{\text{dc}} \quad (4)$$

is briefly considered below, too.

In terms of optics, temporal variable t in Eqs. (1) and (2) is replaced by the propagation distance, z , $g > 0$ is the scaled Kerr coefficient, and coefficient $\kappa(z)$ represents the guiding-antiguinding structure in the bulk material. In that case, a more realistic form of the periodic modulation is piecewise constant, with spatial period $2\pi/\omega$, while the cos term in Eq. (2) represents its first harmonic.

In spite of the presence of the time dependence in Eq. (1), it conserves two dynamical invariants, *viz.*, the norm, proportional to the number of atoms in BEC (or the integral power, in terms of optics),

$$N = \iint dx dy |\psi(x, y)|^2, \quad (5)$$

and the angular momentum,

$$M = i \iint dx dy \psi^* \left(y \frac{\partial}{\partial x} - x \frac{\partial}{\partial y} \right) \psi, \quad (6)$$

where $*$ stands for the complex conjugate. In this work, only states with $M = 0$ are considered. The norm and angular momentum correspond, respectively, to the invariance of Eq. (1) with respect to a phase shift of the wave function and rotation of coordinate system (x, y) .

As concerns the realization of the present model in BEC, an estimate for the atomic condensate of ^7Li atoms, with the scattering length $\simeq -0.1$ nm accounting for the attractive interactions, and the confinement length in the transverse direction $\simeq 1$ μm (which implies the trapping frequency $\simeq 10$ kHz), shows that the length and time units in the scaled variables used in Eq. (1) correspond, respectively, to $\simeq 10$ μm

(which implies the trapping frequency $\simeq 10$ kHz) and 100 ms in physical units, cf. Ref. [19]. In this case, the critical number of atoms leading to the collapse is estimated as 6×10^3 .

In terms of optical waveguides, the use of the carrier wavelength 600 nm in silica leads to a conclusion that the units of the propagation distance and transverse coordinates in scaled equation (1) typically correspond to $\simeq 1$ mm and $15 \mu\text{m}$, respectively, in physical units (cf. Ref. [20]). The corresponding total power of the optical beam may be estimated as $\simeq 3$ MW.

The main issue addressed in this work is to identify conditions under which the TEM scheme based on Eqs. (1) and (2) is able to hold ψ in a robust dynamical state, preventing both the collapse and decay. As mentioned above, this issue is somewhat similar to the problem of identifying conditions for holding a stable 2D soliton by the GPE with periodically sign-flipping self-interaction coefficient, representing the non-linearity management:

$$i \frac{\partial \psi}{\partial t} = -\frac{1}{2} \nabla^2 \psi - g(t) |\psi|^2 \psi, \quad (7)$$

with $g(t) = g_0 + g_1 \cos(\omega t)$, $g_1 > g_0 > 0$, cf. Eqs. (2) and (3) [66–68]. The stability area for 2D quasi-Townes solitons with zero vorticity [i.e., FSs, for which Eq. (6) yields $M = 0$] was identified in the latter model, while all states with nonzero vorticity are unstable (in a two-component system with cross-attraction, a vortex soliton in one component may be stabilized by the FS in the other one [73]). Here we do not consider vortex states governed by Eq. (1), as they should be a subject of a separate work.

Equation (1) can be derived from the Lagrangian,

$$L = \frac{1}{2} \iint dx dy \left[i \left(\psi^* \frac{\partial \psi}{\partial t} + \text{c.c.} \right) - |\nabla \psi|^2 + g |\psi|^4 - \kappa(t) r^2 |\psi|^2 \right], \quad (8)$$

where c.c. stands for the complex-conjugate expression. Following Ref. [74], the VA can be based on the usual Gaussian ansatz,

$$\psi_{\text{ans}}(r, t) = A(t) \exp \left[-\frac{r^2}{2W^2(t)} + i\phi(t) + ib(t)r^2 \right], \quad (9)$$

where real variational parameters are amplitude $A(t)$, width $W(t)$, radial chirp $b(t)$, and phase $\phi(t)$. The conserved norm (5) of the ansatz is

$$N = \pi A^2 W^2. \quad (10)$$

The substitution of ansatz (9) in Lagrangian (8) and integration yields the VA Lagrangian:

$$L_{\text{VA}} = -NW^2 \frac{db}{dt} - N \left(2W^2 b^2 + \frac{1}{2W^2} \right) + \frac{gN^2}{4\pi W^2} - \frac{1}{2} \kappa(t) NW^2. \quad (11)$$

To derive this expression, Eq. (10) was used to eliminate A^2 in favor of W . The first variational (Euler-Lagrange) equation, $\delta L_{\text{VA}} / \delta b = 0$, applied to Lagrangian (11), yields a relation

which expresses the chirp in terms of $W(t)$:

$$b = \frac{1}{2W} \frac{dW}{dt}. \quad (12)$$

The second Euler-Lagrange equation, $\partial L_{\text{VA}} / \partial W = 0$, produces the final dynamical equation, in which Eq. (12) was used to eliminate b :

$$\frac{d^2 W}{dt^2} = \left(1 - \frac{gN}{2\pi} \right) \frac{1}{W^3} - [\kappa_{\text{dc}} + \kappa_{\text{ac}} \cos(\omega t)] W. \quad (13)$$

The TEM term $\sim \kappa_{\text{ac}}$ plays the role of the *parametric drive* in Eq. (13).

The coefficient in front of term $1/W^3$ in Eq. (13) vanishes at the critical point,

$$(gN)_c^{(\text{VA})} = 2\pi. \quad (14)$$

This value is well known as the VA prediction for the TS norm [74], whose numerically found value is $\simeq 7\%$ smaller than (14):

$$(gN)_c^{(\text{num})} \approx 5.85. \quad (15)$$

From now on, we fix, by means of rescaling,

$$N \equiv 1, \quad \kappa_{\text{dc}} \equiv 1 \quad (16)$$

(unless $\kappa_{\text{dc}} = 0$ is fixed in some cases, see below), hence Eqs. (14) and (15) determine the critical values of the self-attraction strength, above which the critical collapse is initiated in the system,

$$g_c^{(\text{VA})} = 2\pi, \quad g_c^{(\text{num})} \approx 5.85. \quad (17)$$

In the case of $g < g_c^{(\text{VA})}$, the constant solution [alias the fixed point (FP)] of the stationary version of Eq. (13), with $\kappa_{\text{ac}} = 0$, is

$$W_{\text{FP}} = \left(1 - \frac{g}{2\pi} \right)^{1/4}, \quad (18)$$

where normalization (16) is taken into regard. This solution is obviously stable, as it realizes a minimum of the respective Hamiltonian, in the case of $\kappa_{\text{ac}} = 0$. The frequency of small oscillations around the FP does not depend on g ,

$$\Omega_{\text{FP}} = 2, \quad (19)$$

as long as it falls below the critical value, $g < 2\pi$, see Eq. (17).

This analysis can be readily extended to the case of $\kappa_{\text{ac}} \neq 0$, provided that the modulation frequency ω is large, by means of the averaging method, cf. Ref. [75]. In this case, an approximate solution to Eq. (13) is looked for as

$$W(t) = W^{(0)}(t) + W^{(1)} \cos(\omega t), \quad (20)$$

where $W^{(0)}(t)$ is a slowly varying term, and the harmonic balance yields

$$W^{(1)} = (\kappa_{\text{ac}} / \omega^2) W^{(0)}. \quad (21)$$

Then, the substitution of expressions (20) and (21) in Eq. (13) leads to an effective equation for the slow evolution of $W^{(0)}(t)$:

$$\frac{d^2 W^{(0)}}{dt^2} = \left(1 - \frac{gN}{2\pi} \right) \frac{1}{[W^{(0)}]^3} - \left(1 + \frac{\kappa_{\text{ac}}^2}{2\omega^2} \right) W^{(0)}. \quad (22)$$

The respective FP value changes from the one given by Eq. (18) to

$$W_{\text{FP}} \approx \left(1 - \frac{g}{2\pi}\right)^{1/4} \left(1 - \frac{\kappa_{\text{ac}}^2}{8\omega^2}\right), \quad (23)$$

and frequency (19) of small oscillations around the FP is replaced by

$$\Omega_{\text{FP}} \approx 2 \left(1 + \frac{\kappa_{\text{ac}}^2}{4\omega^2}\right), \quad (24)$$

where the smallness of ω^{-2} is taken into regard. On the other hand, the correction induced by rapid oscillations does not affect the VA-predicted collapse threshold given by Eq. (17)

The nonexistence of solution (18) at $g > 2\pi$ in the case of $\kappa_{\text{ac}} = 0$ signals the transition to the collapse. In this case, the onset of the collapse is described by a simple solution of Eq. (13) with $\kappa_{\text{dc,ac}} = 0$ (recall $N = 1$ is fixed):

$$W(z) = W_0 \sqrt{1 - t/t_{\text{coll}}}, \quad (25)$$

where W_0 is the initial width, and the VA-predicted collapse time is

$$t_{\text{coll}} = \frac{2W_0^2}{\sqrt{g/(2\pi) - 1}}. \quad (26)$$

If the action of the ac component in Eq. (13) gives rise to instability through excitation of the PR, then development of the instability implies that the amplitude of oscillations of $W(t)$ grows, hence the term $\sim W^{-3}$ in Eq. (13) becomes negligible. The corresponding linear equation is the classical Mathieu equation [76]:

$$\frac{d^2W}{dt^2} = -[\kappa_{\text{dc}} + \kappa_{\text{ac}} \cos(\omega t)]W. \quad (27)$$

The commonly known instability chart of Eq. (27) in the plane of $(\kappa_{\text{ac}}, \omega)$ (see, e.g., Ref. [78]) is determined by the fundamental and higher-order PRs [77]. In the limit of $\kappa_{\text{ac}} \rightarrow 0$, the PRs of orders $m = 0, 1, 2, \dots$ take place at values of the driving frequency

$$\omega_{\text{PR}}^{(m)} = 2/(1 + m), \quad (28)$$

the fundamental (strongest) PR corresponding to $m = 0$, i.e., $\omega_{\text{PR}}^{(0)} = 2$.

The relation between Eqs. (13) and (27) is not surprising, as Eq. (13) belongs to the class of the Ermakov's equations [79–84]. In this context, it is well known that a general solution of Eq. (13), $W(t)$, may be exactly expressed in terms of two independent solutions, $w_1(t)$ and $w_2(t)$, of the Mathieu equation (27), and their constant Wronskian, as follows:

$$\frac{W^2(t)}{\sqrt{1 - g/(2\pi)}} = w_1^2(t) + \left(\frac{w_2(t)}{\text{Wronskian}\{w_1(t), w_2(t)\}} \right)^2. \quad (29)$$

Thus, Eq. (29) corroborates that the onset of the instability in solutions of the Mathieu equation implies, in the exact form, that the solutions of the Ermakov equation (13) also becomes unstable.

III. NUMERICAL RESULTS

A. The formulation of the problems

First, stationary solutions of Eq. (1), without the ac drive ($\kappa_{\text{ac}} = 0$) and with $g < g_c^{(\text{num})} \approx 5.85$ [see Eq. (17)], were produced numerically by means of the well-known imaginary-time integration method [85–87]. Then, using the stationary solutions as inputs, we performed simulations of GPE (1) in the full form, including the ac drive by means of the standard split-step fast-Fourier-transform algorithm [87]. The drive's parameters, κ_{ac} and ω , were varied with the aim to identify stable and unstable dynamical states in the course of the long-time evolution. One of the main objectives of this work being to explore the possibility of finding stable ac-driven FSs at $g > g_c^{(\text{num})}$, when no stationary solution exists in the absence of the ac drive, the input in this case was taken as the normalized Gaussian,

$$\psi(r, t = 0) = \sqrt{1/\pi} \exp(-r^2/2). \quad (30)$$

The simulations were performed in the domain of size 12×12 , with the spatial mesh size $\Delta x = \Delta y = 0.03$ (i.e., the integration domain was covered by the mesh composed of 400×400 points) and the time step $\Delta t = 0.0001$. A boundary absorber was inserted in the simulations to prevent irrelevant perturbation of the dynamical state by waves reflected from the domain's boundary.

The dynamics of the FS mode under the action of TEM may be adequately characterized by time dependencies of its height and width, i.e., the (peak) density at the center, $|\psi(r = 0, t)|^2$, and the monopole moment, which determines the average radial size of the mode,

$$\langle r \rangle(t) = N^{-1} \iint |\psi(x, y)|^2 \sqrt{x^2 + y^2} dx dy \quad (31)$$

[in fact, we set $N \equiv 1$, see Eq. (16)]. Also essential are spectra of the Fourier transform of the central density and radial size, computed as

$$\begin{aligned} \hat{n}(\Omega) &= \left| \int_0^T e^{-i\Omega t} |\psi(r = 0, t)|^2 dt \right|, \\ \hat{r}(\Omega) &= \left| \int_0^T e^{-i\Omega t} \langle r \rangle(t) dt \right|, \end{aligned} \quad (32)$$

for a long simulation interval T . Note that, in terms of the VA ansatz, represented above by Eqs. (9), (10), and (16), these characteristics are given by

$$|\psi(r = 0, t)|^2 = (\pi W^2)^{-1}, \quad \langle r \rangle = (\sqrt{\pi}/2)W. \quad (33)$$

The boundary of the PR-induced instability, produced by systematic simulations of GPE (1), is then compared to its counterpart predicted by the VA, based on simulations of the Ermakov equation (13). Those long-time simulations start with the input taken as per Eq. (18).

B. The stability boundary of the FS against the PR under the action of the TEM

First, Fig. 1 represents a typical example of fully robust evolution of the FS under the action of TEM, with $\omega = 4$ and $\kappa_{\text{ac}} = 2$ exceeding 1, hence the sign of the quadratic potential

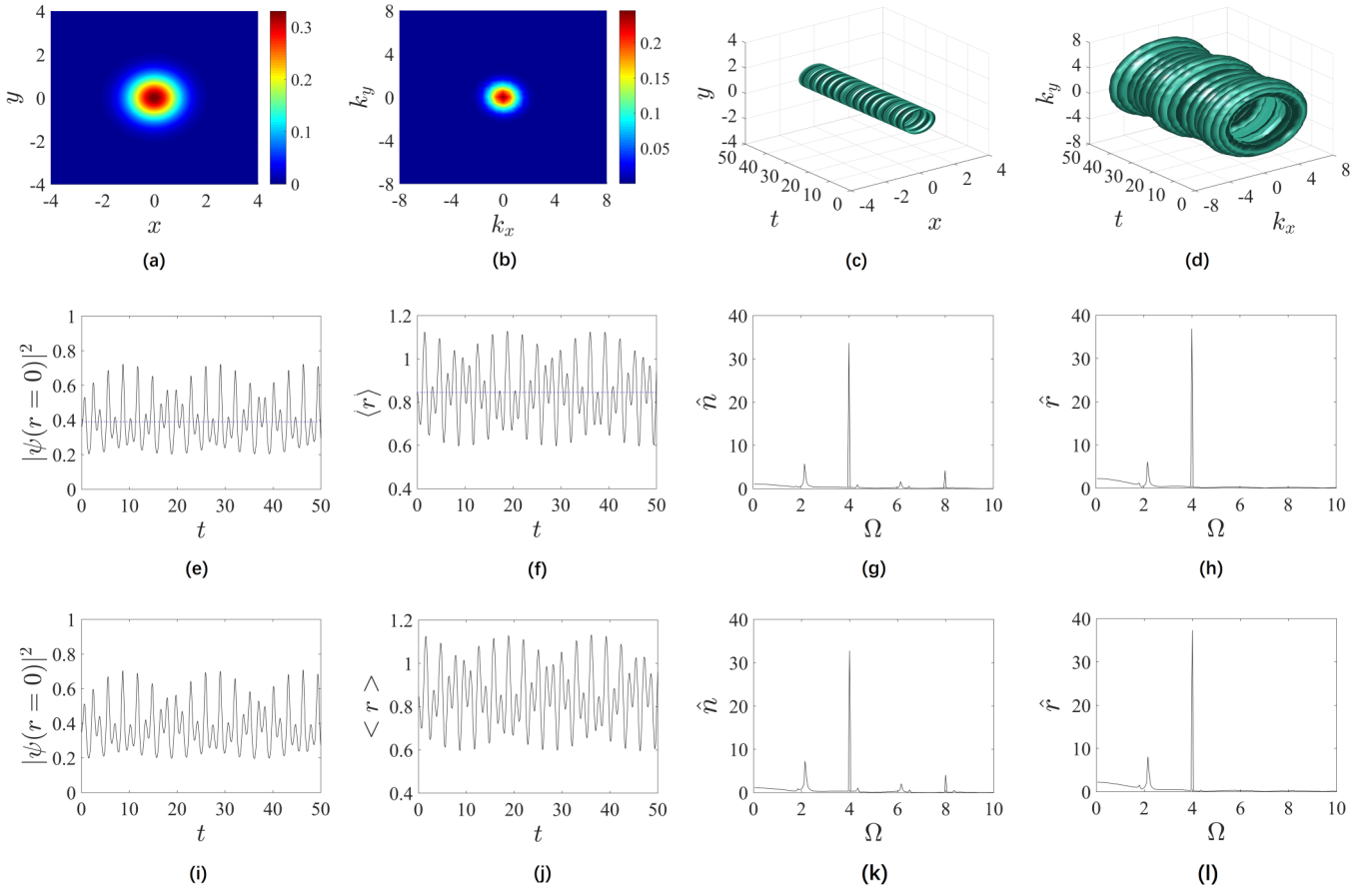


FIG. 1. An example of stable dynamics of the FS governed by Eqs. (1) and (16), with $g = 1$, $\kappa_{ac} = 2$, and $\omega = 4$. (a) The input density pattern (34), taken as per the stationary solution of Eq. (1) with $\kappa \equiv 1$. (b) The spatial Fourier transform of (a), defined according to Eq. (35). [(c) and (d)] The evolution of the density profile and its spatial Fourier transform. [(e) and (f)] The corresponding evolution of the peak density, $|\psi(r = 0, t)|^2 \equiv n(t)$, and monopole moment (radial size), defined as per Eq. (31). Dashed horizontal lines in panels (e) and (f) show average values of the corresponding variables. [(g) and (h)] The temporal Fourier transform of the peak density, $\hat{n}(\Omega)$, and radial size, $\hat{r}(\Omega)$, calculated as per Eq. (32) with $T = 500$. Panels (i)–(l) demonstrate the results corresponding to those in (e)–(h), as produced by the VA.

in Eq. (1) indeed periodically flips, according to Eq. (2). This figure is produced for $g = 1$, which is far from the critical value (17). Figures 1(a) and 1(b) display the pattern of the local density in the input [stationary solution of Eq. (1) with $\kappa_{ac} = 0$],

$$n(x, y) = |\psi(x, y)|^2, \quad (34)$$

and its Fourier transform,

$$\begin{aligned} \hat{n}(k_x, k_y) &= \iint \exp[-i(k_x x + k_y y)] n(x, y) dx dy \\ &\equiv 2\pi \int_0^\infty n(r) J_0(kr) r dr, \end{aligned} \quad (35)$$

where it is taken into regard that n depends only on the radial coordinate, $k = \sqrt{k_x^2 + k_y^2}$, and J_0 is the Bessel function. Further, the periodic evolution of the density and its Fourier transform in the numerically generated solution with $\kappa_{ac} = 2$ is displayed in Figs. 1(c) and 1(d), respectively.

Naturally, the peak density, $n(r = 0)$, and radial size (31) of the solution with $\kappa_{ac} = 2$ feature antiphase oscillations in Figs. 1(e) and 1(f). The spectrum of the oscillations, displayed in Figs. 1(g) and 1(h), features the main peak at the driving

frequency, $\omega = 4$, a weak subharmonic peak at $\omega = 2$, a weak one at the double frequency, $\omega = 8$, and an additional very weak but visible peak at the combinational sesquilateral harmonic, $\omega = 6$. Furthermore, comparison of Figs. 1(i)–1(l) and 1(e)–1(h) demonstrates close agreement between the simulations of the full GPE and their VA-produced counterparts. It has been also checked that, in the case of the stability, full simulations of the underlying GPE always conserve the total norm (10) of the wave function.

The structure of the oscillatory states shown in Fig. 1 is typical for relatively large values of the driving frequency ω . At small values of ω , it may be essentially different: In addition to the main low-frequency peak at $\Omega = \omega$, the spectrum features a somewhat weaker but conspicuous one at a much larger frequency, $\Omega \simeq 2$, which is easily predicted by Eq. (19), in the case when ω is small. Examples of this are displayed in Fig. 2, in which the top and middle rows show, respectively, the time dependence of the FS's radial size, $\langle r \rangle(t)$, and its spectral counterpart, $\hat{r}(\Omega)$, as obtained from the simulations of GPE (1). In addition, the bottom row shows $\hat{r}(\Omega)$ as produced by the VA. Typical examples of the low-frequency cases, with $(\omega, \kappa_{ac}) = (0.5, 0.2)$ and $(\omega, \kappa_{ac}) = (0.1, 0.2)$, are presented, respectively, in columns (C1)–(C3) and (D1)–(D3). Note that

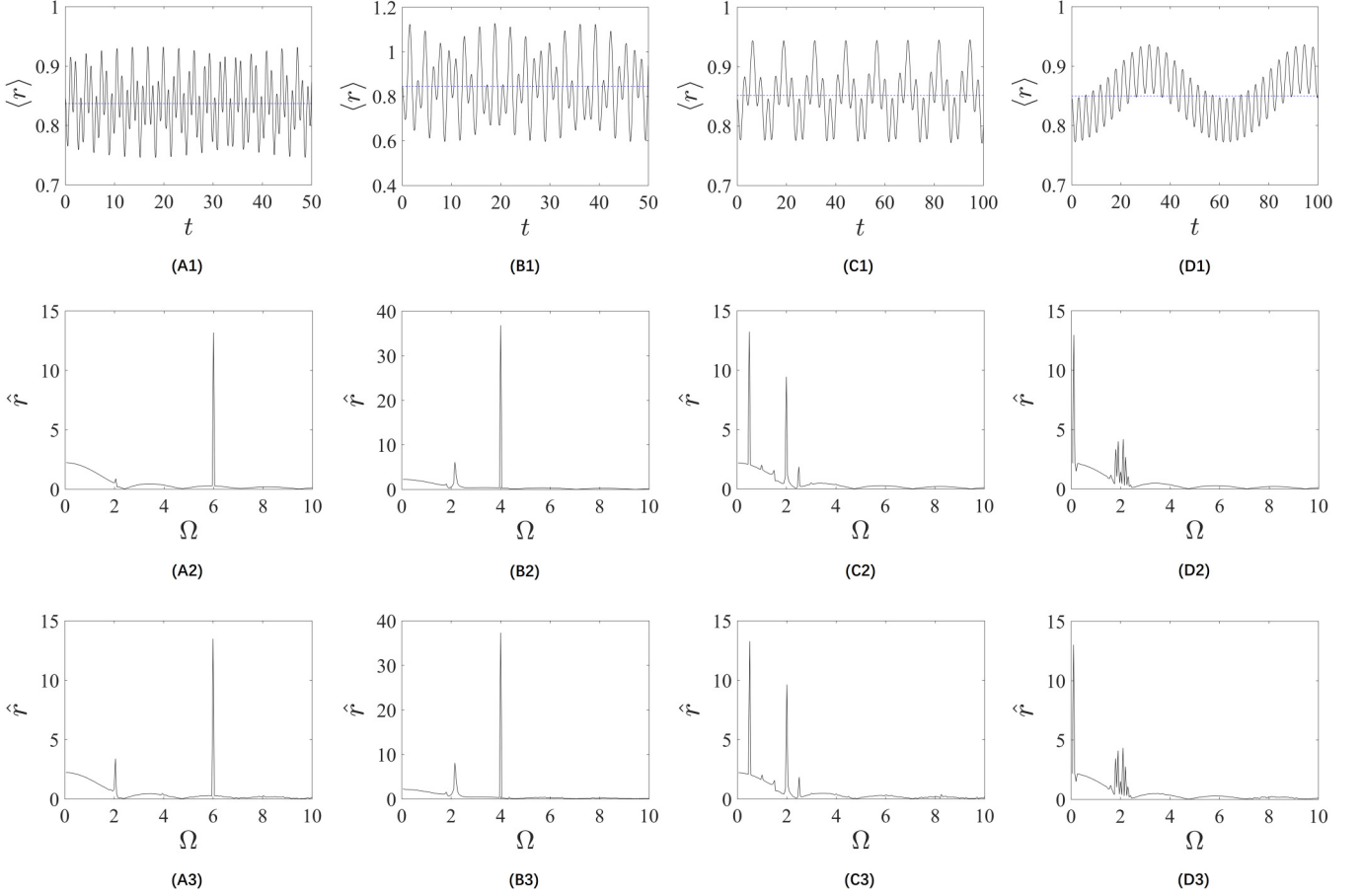


FIG. 2. Panels (A1)–(D1): The radial size [monopole moment, see Eq. (31)] vs. time, produced by the simulations of Eq. (1). (A2)–(D2): The respective spectra. (A3)–(D3): The spectra as produced by the VA. The parameters are $(\kappa_{ac}, \omega) = (2, 6)$ in (A1)–(A3); $(2, 4)$ in (B1)–(B3); $(0.2, 0.5)$ in (C1)–(C3); and $(0.2, 0.1)$ in (D1)–(D3). In all plots, $(g, \kappa_{dc}) = (1, 1)$. At $\omega > 2$, the main peak in the spectra, produced by the GPE and VA alike, is at $\Omega = \omega$. At $\omega < 2$, there is an additional major spectral peak close to $\Omega = 2$ [it is split in subpeaks in panels (D2) and (D3)].

the peak at $\Omega \simeq 2$ in panels (D2) and (D3) is split into subcomponents by combinations of the main one with those corresponding to the small driving frequency ω [a weak combinational peak at $\Omega = 2 + \omega$ is observed as well in panels (C2) and (C3)]. The oscillatory states displayed in columns (C1)–(C3) and (D1)–(D3) are akin to breathers which are represented, in the framework of the VA, by oscillatory solutions of Eq. (13) in the absence of the ac drive, i.e., with $\kappa_{ac} = 0$.

For the comparison's sake, columns (A1)–(A3) and (B1)–(B3) in Fig. 2 represent typical high-frequency cases, with $(\omega, \kappa_{ac}) = (2, 6)$ and $(\omega, \kappa_{ac}) = (2, 4)$, respectively. Note that the corresponding spectra also include peaks at $\Omega \approx 2$, although small-amplitude ones. Furthermore, a small but visible shift of these peaks to values of Ω slightly larger than 2 in Figs. 2(B2) and 2(B3) is readily explained by Eq. (24).

A typical example of the PR-driven instability of the ac-driven FS is displayed in Fig. 3. This example is produced for $\omega = 2$, which directly corresponds to the fundamental PR, as given by Eq. (28) with $n = 0$. It is seen that both full simulations of the underlying GPE (1) and the corresponding numerical solution of the variational equation (13) lead to decay of the trapped FS, which takes place after several oscillations with an increasing amplitude, in the interval of time

which is identified, approximately, as $0 < t < 7.5$. At $t \approx 7.5$, the expanding FS hits the region where the above-mentioned edge absorber is installed. The GPE simulations can be extended to larger times, but the results are then essentially affected by the loss inflicted by the absorber. In any case, the onset of the PR-induced instability is adequately revealed by the GPE simulations at the stage which is not affected by the absorber. The same is true as concerns the onset of the instability at other values of parameters.

Results produced by the systematic simulations of GPE (1) at different values of parameters ω , κ_{ac} , and g (including both $g > 0$ and $g < 0$, i.e., the self-attractive and repulsive nonlinearity) are collected in the form of the stability diagrams shown in Fig. 4. The ac-driven FS is stable beneath the boundaries shown in the left bottom corner of the plots and above boundaries in their top parts. First, point $\omega = 2$ at which the instability area emerges is explained by the fundamental PR, which is predicted by Eq. (28) with $n = 0$. Further, a relatively short segment of the bottom boundary at $\omega \approx 1$ is explained as a manifestation of the next-order PR corresponding to $n = 1$ in Eq. (28). The instability does not occur at very large values of ω . This case can be considered by means of the above-mentioned averaging method, which does not demonstrate any source of instability, cf. Ref. [75].

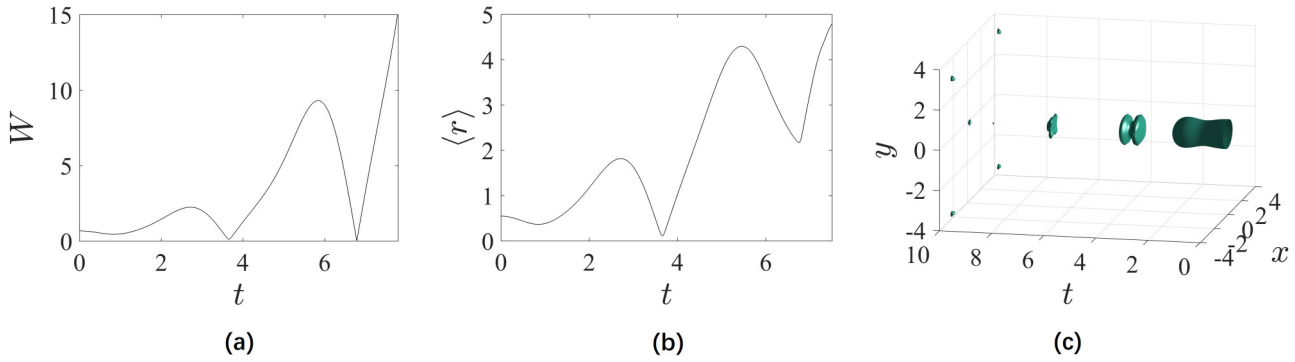


FIG. 3. A typical example of the evolution of an unstable FS under the action of TEM with parameters $(g, \kappa_{ac}, \omega) = (5, 2, 2)$. Results of simulations of the VA-produced Ermakov equation (13) and of GPE (1) are displayed, respectively, in panels (a) and then (b) and (c). In panel (a) it is seen that, after several oscillations of the width with an increasing amplitude, fast expansion of the wave function commences. Panels (b) and (c) display essentially the same outcome of the evolution, by means of the time dependence of $\langle r \rangle(t)$ and density profile.

Figure 4 shows that the dependence of the stability boundaries on the strength and sign of the nonlinearity [in particular, in Fig. 4(a), which shows the results for $g = \pm 5$] is very weak, including values of g in Fig. 4(b) which are close to the collapse threshold, cf. Eq. (17). In this connection, it is relevant to recall that, in the framework of the nonlinear Ermakov equation (13), the boundary of the PR-induced instability indeed does not depend on the nonlinearity strength, being identical to that in the linear Mathieu equation (27). Actually, an essential result demonstrated by Fig. 4 is that the full GPE (1), for which the VA equations (13) and (27) are only an approximation, produces a visible but very weak dependence of the boundary on g , i.e., the approximation is quite accurate, in this sense.

Note that the stability diagrams displayed in Fig. 4 include not only values $\kappa_{ac} > 1$, for which the sign of the quadratic potential in Eq. (1) periodically flips, but also $\kappa_{ac} < 1$, for which the potential always keeps the trapping sign. Accordingly, the system is more robust in the latter case [usually, only this case is considered in the framework of the Mathieu equation (27)].

Indeed, the bottom stability area in all panels of Fig. 4 exists solely at $\kappa_{ac} < 1$.

The stability boundaries, as produced by the systematic simulations of the GPE (1) and by the numerical solution of the VA-produced Ermakov equation (13), are compared in Fig. 5, by juxtaposing them in the plane of (κ_{ac}, ω) for $g = 0, 1$, and ± 5 . It is seen that the VA always provides a reasonable agreement with the full GPE, and becomes very accurate for larger values of g .

C. The boundary of the critical collapse

A typical example of the solution which quickly develops the collapse at $g = 7$, that definitely exceeds the largest value admitting the stability of the FS, is displayed in Fig. 6. The blowup of the solution is obvious. In particular, its VA-predicted width shrinks to zero at the collapse moment, cf. the VA-predicted solution for the collapse in the absence of the HO potential, given by Eqs. (25) and (26). In this case, the

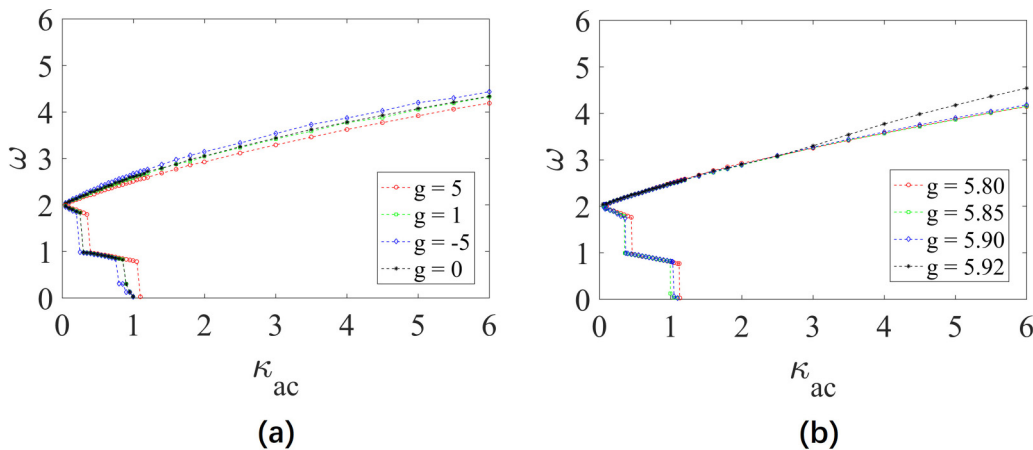


FIG. 4. The stability diagram in the (κ_{ac}, ω) plane for the ac-driven FS, as produced by systematic simulations of GPE (1). The instability takes place between the top and bottom boundaries. (a) A set of boundaries for $g = \pm 5$ and $g = 0, 1$, which includes both the self-attractive and repulsive signs of the nonlinearity, as well as the linear system ($g = 0$). (b) A set of the stability diagrams for values of g close to the threshold of the critical collapse, at which the instability is still determined by the PR (not by the proximity to the collapse).

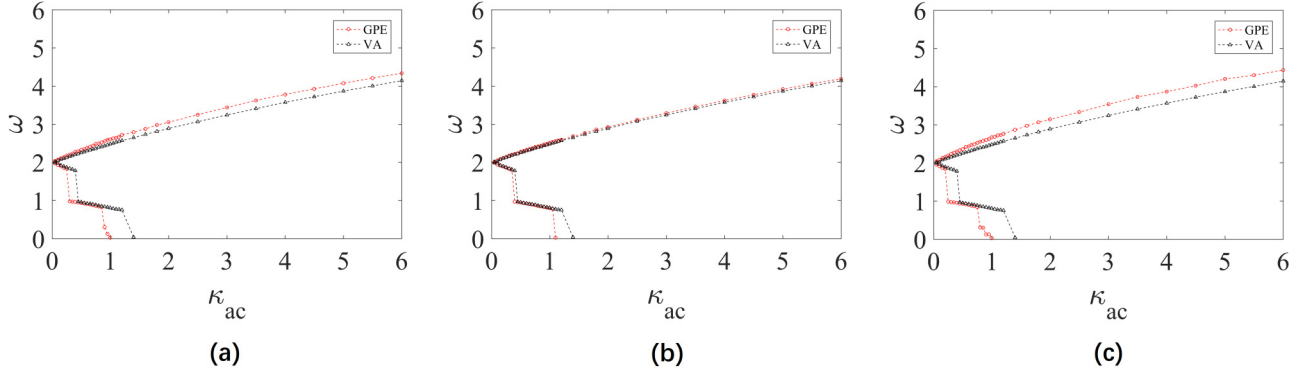


FIG. 5. Stability boundaries in the plane of (κ_{ac}, ω) , as produced by the simulations of the GPE in the form of Eqs. (1) and (2), and by the numerical solution of the VA-predicted Ermakov equation (13). The nonlinearity coefficient is $g = 0$ in (a) (i.e., the system is linear), $g = 5$ in (b), and $g = -5$ in (c).

collapse takes place after the evolution time

$$t_{\text{collapse}}^{(\text{VA})} \approx 0.64; t_{\text{collapse}}^{(\text{numer})} \approx 0.76 \quad (36)$$

in the framework of the VA or GPE simulations, respectively, which is essentially smaller than the TEM period, $2\pi/\omega \approx 1.57$, i.e., the time modulation of the trapping potential does not essentially affect the onset of the collapse.

Because, as mentioned above, the difference between the numerically exact and VA-predicted values of the self-attraction strength at the point of the onset of the critical collapse, in the absence of TEM, is conspicuous, $[g_c^{(\text{VA})} - g_c^{(\text{num})}]/g_c^{(\text{VA})} \simeq 7\%$, as per Eq. (17), the VA is not appropriate for accurate identification of the shift of g_c under the action of TEM. This was done by means of systematic simulations of GPE (1) with the HO strength taken according to Eq. (2). An example of the implementation of this approach is displayed in Fig. 7. It shows that the time-average (mean) values of the peak density and radial size of the ac-driven SF monotonously grow and decrease, respectively, with the increase of g , passing the value $g_c^{(\text{num})} \approx 5.85$, which corresponds to the usual TS [see Eq. (17)], and attaining the critical point at $g_c \approx 5.938$, at which the solution suffers the blowup.

The development of the collapse at a point which is almost exactly tantamount to the critical one is displayed in Fig. 8. Due to the action of the TEM, the collapse takes place after a few cycles of compression and expansion of the FS.

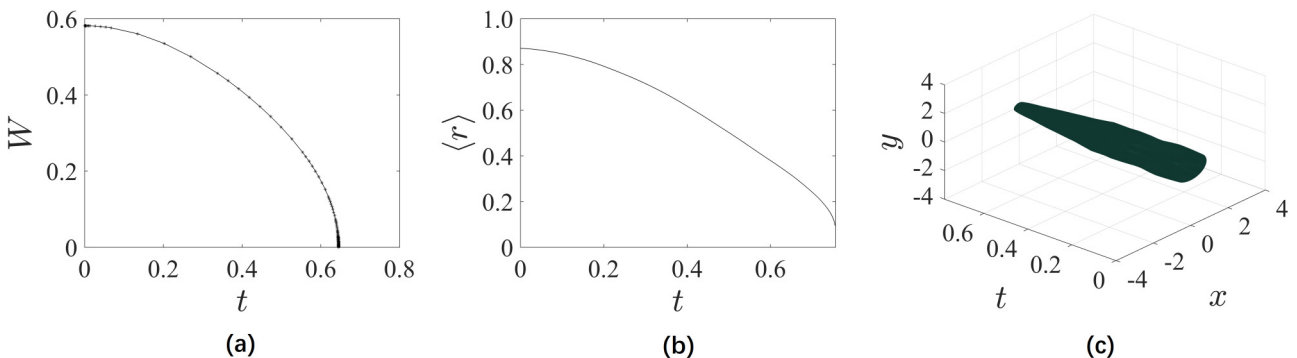


FIG. 6. A typical example of the evolution of a collapsing FS obtained for parameters $(g, \kappa_{ac}, \omega) = (7, 2, 4)$. (a) The shrinking width, $W(t)$, as predicted by the VA, i.e., by the Ermakov equation (13). [(b) and (c)] The shrinkage of the FS as produced by the simulations of GPE (1). The plots in panels (a), (b), and (c) are cut, respectively, at times indicated in Eq. (36).

In Fig. 9 we plot the boundary of the onset of the collapse in the plane of (κ_{ac}, ω) , for three values of the self-attraction strength g exceeding the usual critical value ≈ 5.85 [see Eq. (17)], as produced by the systematic simulations of Eqs. (1) and (2). A characteristic difference between the boundary determined by the onset of the critical collapse, and the boundary of the PR-induced instability plotted in the same parametric plane at $g < g_c$ (cf. Figs. 4 and 5), is that the collapse boundary shrinks to one or two segments, no stable FS existing outside of them.

Finally, the most important characteristic of the partial stabilization of the FS modes by TEM at

$$g > g_c^{(\text{num})} \approx 5.85 \quad (37)$$

is presented by Fig. 10, which shows the critical value g_c of the self-attraction strength, at which the solutions suffer the blowup, vs. ω and κ_{ac} . Similarly to the situation observed in Fig. 9, the dependencies feature gaps, in which the blowup commences at essentially lower values of g . The largest value of g_c produced by the systematic simulations is $(g_c)_{\text{max}} \approx 5.938$.

Note that the results summarized in Figs. 9 and 10 are obtained for both cases of $\kappa_{ac} < 1$ and $\kappa_{ac} > 1$. Generally, the latter case is more favorable for the expansion of the stability region into the nontrivial area (37), unless ω is too small (in particular, Fig. 9 shows no stability regions at $\kappa_{ac} < 1$). These

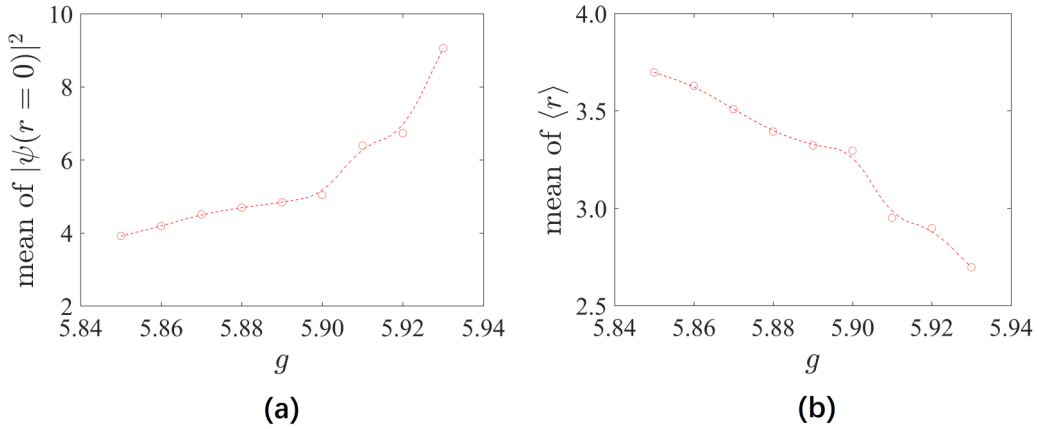


FIG. 7. Dependencies of mean (time-average) values of the density at the central point (a) and radial size (b), produced by simulations of Eq. (1) and (2) with $\kappa_{ac} = 2$ and $\omega = 4$, on the self-attraction strength, g . The dependencies terminate at the collapse point, $g_c \approx 5.938$. This value exceeds the standard one, $g_c \approx 5.85$, corresponding to the usual TSS, see Eq. (17).

trends can be understood, as Eq. (2) with $\kappa_{ac} > 1$ implies the periodic switching from the trapping (HO) potential to the expulsive (anti-HO) one. Naturally, the anti-HO potential tends to arrest the evolution toward the blowup at $r = 0$. This feature can be demonstrated in an approximate form by the fact that Eq. (13) (in which $N = 1$ is set, as above), with $\kappa_{dc} + \kappa_{ac} \cos(\omega t)$ replaced by a constant *negative* value of κ , admits an FP solution in the case when g exceeds the respective critical value, $g_c^{(VA)} = 2\pi$ [see Eq. (17)]:

$$W_{FP} = \left[-\frac{1}{\kappa} \left(\frac{g}{2\pi} - 1 \right) \right]^{1/4}, \quad (38)$$

cf. stationary solution (18). Of course, the FP given by Eq. (38) is, by itself, unstable, unlike its counterpart (18), but its appearance helps to understand how TEM makes the FS more robust against the collapse. On the other hand, this mechanism is not efficient for low ac-driving frequencies ω , as the corresponding time $\sim \pi/\omega$, needed for the switch between the HO and anti-HO potentials, may be larger than the collapse time, which is approximately given by Eq. (26).

A typical example of an FS found in the nontrivial stability area (37), *viz.*, at $g = 5.90$, is displayed in Fig. 11.

The dynamical structure of such states is generally similar to that presented in Fig. 2 for $g = 1$. Characteristic examples, for the same cases of the low- and high-frequency ac drive as those in Fig. 2, are displayed in Fig. 12. Like in Fig. 2, the spectrum features two main peaks, at $\Omega = \omega$ and $\Omega \simeq 2$. The latter one, predicted by Eqs. (19) and (24), features a split shape in the case of the low-frequency drive. On the other hand, a difference is that the time dependencies of the peak density and radial size, as well as the respective spectra, demonstrate robust but irregular oscillations in Fig. 12, unlike the quasiregular dynamical regimes revealed by Fig. 2.

A noteworthy peculiarity of Figs. 10(a) and 10(b) is that the nontrivial stability region (37) exists, up to $g \approx 5.93$, even in the limit cases of $\omega = 0$ and $\kappa_{ac} = 0$, when the ac drive is not present. In this case, simulations of Eq. (1), with the input taken as a stationary FS numerically found at $g \leq g_c^{(num)} \approx 5.85$, lead to the collapse, as it might be expected. However, the input (30) produces oscillatory states (breathers) which, unlike the collapsing quasistationary states, may indeed keep their dynamical stability up to $g \approx 5.93$. An example of such a dynamical regime, produced by the simulations of Eq. (1) with $g = 5.90$ and $\kappa_{ac} = 0$, is presented in Fig. 13. In particular, the power spectrum observed in Fig. 13(c) is typical for

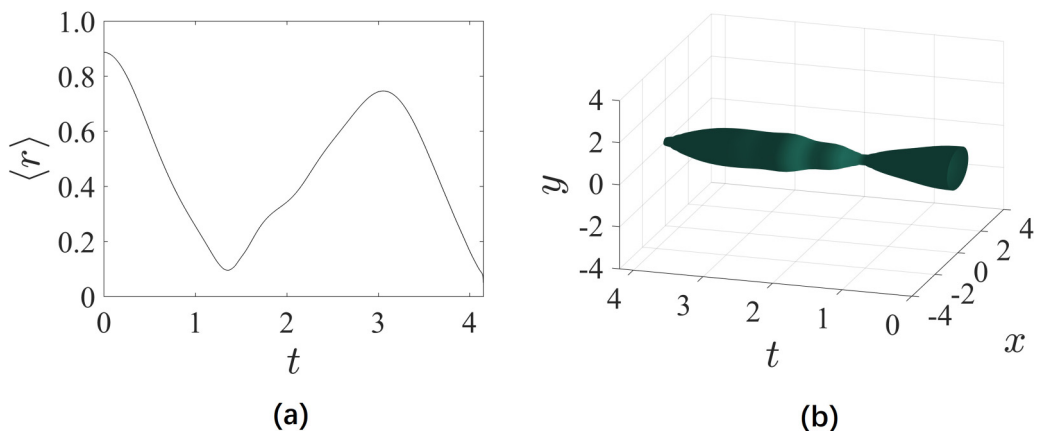


FIG. 8. Panels (a) and (b) display the same as in Figs. 6(b) and 6(c) but for parameters $(g, \kappa_{ac}, \omega) = (5.938, 2, 4)$.

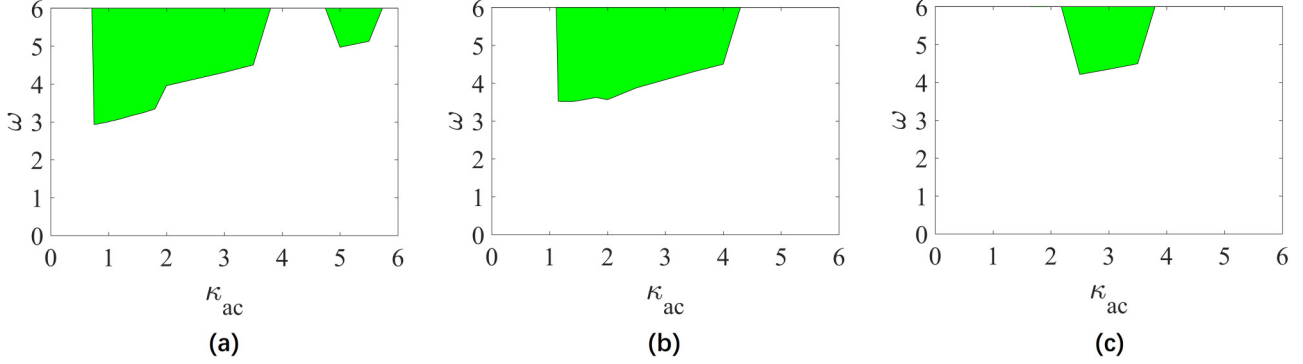


FIG. 9. Stability diagrams in the plane of (κ_{ac}, ω) at values of the self-attraction strength, g , exceeding the usual critical value, $g_c^{(\text{num})} \approx 5.85$, see Eq. (17). Stable FSs are produced by simulations of Eqs. (1) and (2) in green areas. Fixed values of g are 5.933 in (a), 5.935 in (b), and 5.937 in (c).

oscillations in autonomous nonlinear dynamical systems, being different from that for the ac-driven system, cf. Fig. 11(e).

IV. CONCLUSION

The aim of this work is to elaborate a scheme of TEM, which helps to stabilize 2D FS (fundamental-state) modes under the action of the cubic self-attraction, that gives rise to the critical collapse in the 2D space, thus making the usual TSs completely unstable. The TEM scheme works by applying the quadratic potential with the periodically flipping sign, so that it switches between the trapping HO and expulsive anti-HO forms. The TEM scenario can be realized in nonlinear optics and in BEC. The analysis of the FS dynamics under the action of TEM is performed by means of systematic simulations, in the combination with the VA. The VA reduces the FS dynamics to an equation of the Ermakov type. Stability boundaries for the FS trapped in the periodically switching potential have been identified, as functions of strength g of the cubic self-attraction, and amplitude and frequency of the ac (time-periodic) part of the potential's strength. Below the standard (Townes) collapse threshold, which means $g < g_c^{(\text{num})} \approx 5.85$ in the notation adopted here, the stability area is bounded by

the onset of the fundamental or higher-order PR. This boundary is well approximated by the VA, including the system with the self-repulsive nonlinearity, $g < 0$, and the linear one ($g = 0$). At $g > g_c$, the collapse boundary is identified for FSs by means of systematic simulations of the underlying GPE. The largest value of the self-attraction strength, which admits the stability against the critical collapse in the system, is $g \approx 5.938$, exceeding the standard one, $g_c^{(\text{num})} \approx 5.85$, by $\approx 1.5\%$. This increase, although relatively small, is a significant result, as the standard collapse threshold is usually strictly fixed. The extension of the stability region above $g_c^{(\text{num})} \approx 5.85$ takes place also in the absence of the TEM. It is explained by the fact that a breather, in the form of an oscillatory FS, may keep its stability against the collapse at values of g which are somewhat larger than 5.85.

The obtained results can be verified in experiments, and, as concerns the implementation in optics, they may find applications to the design of photonic devices based on waveguide-antiwaveguide schemes.

A natural direction for the continuation of the work is the development of the analysis for 2D states with intrinsic vorticity, which will be reported elsewhere. Another possibility is the consideration of TEM in the 1D system with

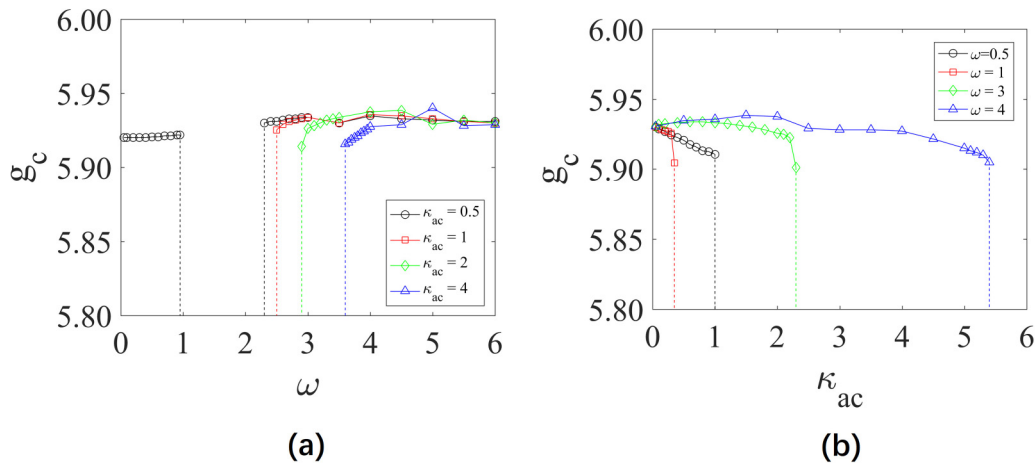


FIG. 10. (a) The critical value, g_c , of the self-attraction strength, g , at which the trapped FS is destroyed by the blowup, vs. the driving frequency, ω , at several fixed values of ac-drive's amplitude, κ_{ac} . (b) The same for g_c as a function of κ_{ac} at fixed values of ω . Gaps in which the dependencies are not displayed are regions in which g_c falls to essentially lower values.

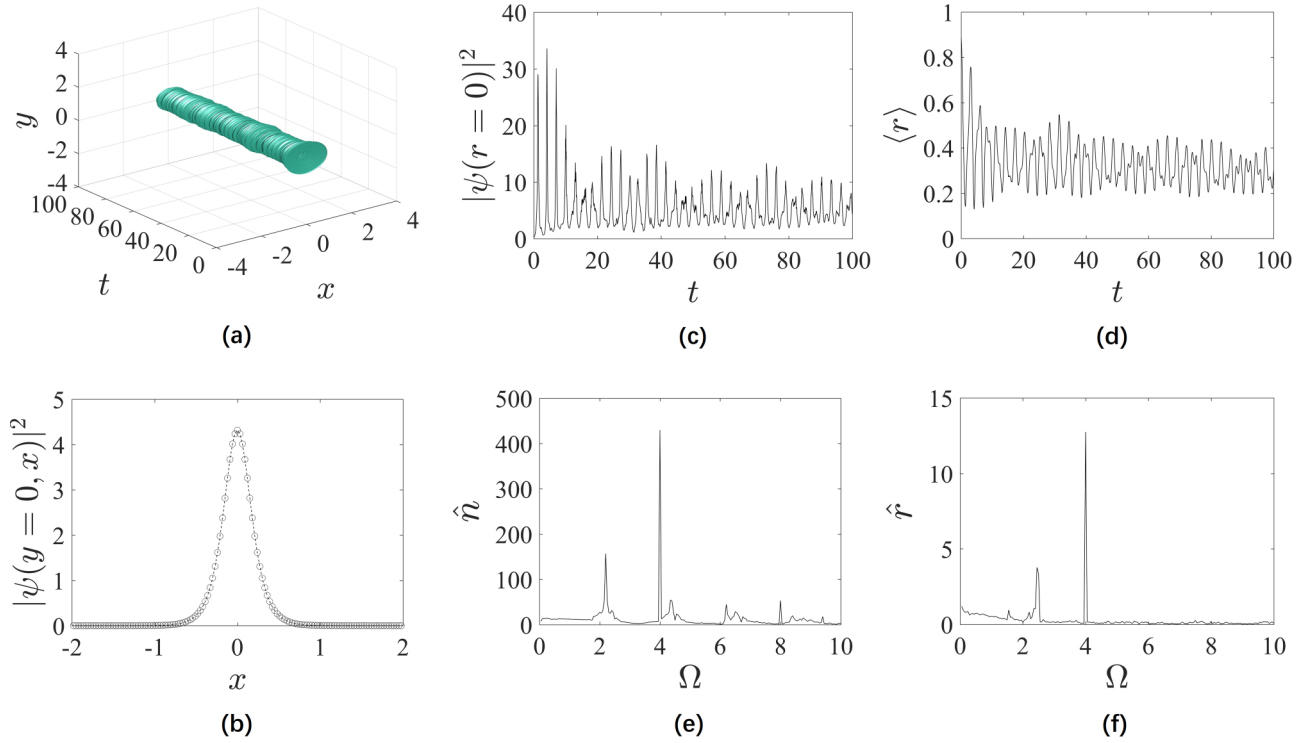


FIG. 11. A typical stable FS found in region (37), at parameters $(g, \kappa_{dc}, \kappa_{ac}, \omega) = (5.90, 1, 2, 4)$. The solution is produced by simulations of Eq. (1) with input (30). (a) The spatiotemporal density profile. (b) The cross section of the spatial profile, $|\psi(y=0, x)|^2$ at $t = 100$. [(c) and (d)] The evolution of the peak power, $|\psi(x=y=0, t)|^2$, and effective radius (31). [(e) and (f)] Spectra of the Fourier transform of the same variables, defined as per Eq. (32).

the quintic self-attraction, which gives rise to the TSs and critical collapse in 1D [88–90]. It may also be interesting to consider the 2D model which includes, as an additional stabilizing ingredient, a permanent anharmonic (quartic) term in the trapping potential. Such a term was considered in the context of BEC in various settings [91–94].

ACKNOWLEDGMENTS

This work was supported by NNSFC (China) through Grant No. 1187411211905032, Natural Science Foundation of Guangdong province through Grant No. 2021A1515010214, Key Research Projects of General

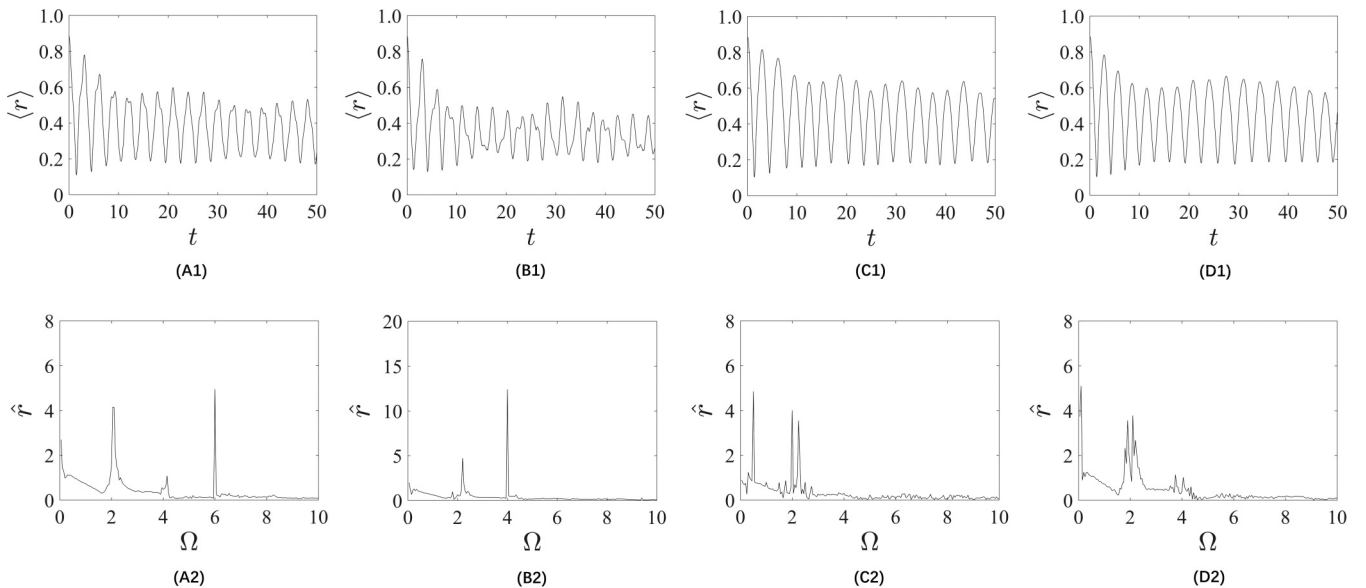


FIG. 12. The same as in Figs. 2(A1)–2(D1) and 2(A2)–2(D2) but for $(g, \kappa_{dc}) = (5.90, 1)$. Note that the solution displayed in panels (B1) and (B2) is the same as shown in Fig. 11. It is included here for the comparison's sake.

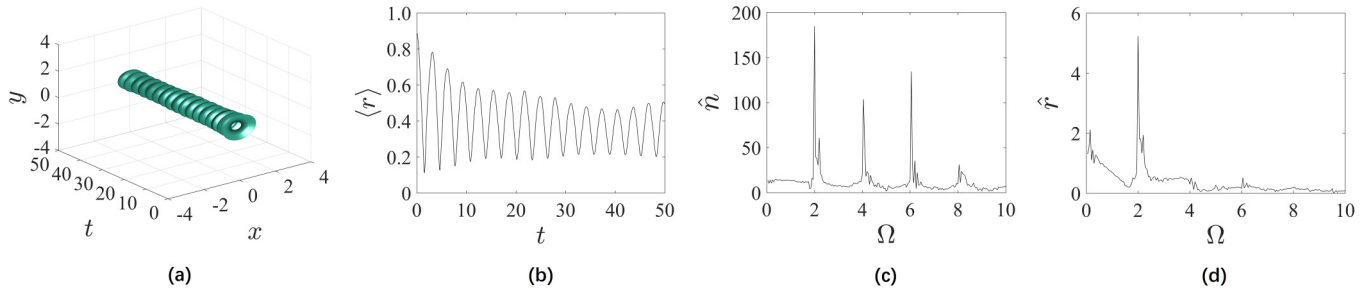


FIG. 13. The stable evolution of a breather in the absence of the ac drive in Eq. (1), with parameters $(g, \kappa_{dc}, \kappa_{ac}) = (5.90, 1, 0)$. (a) The evolution of the density profile. (b) The evolution of the monopole moment (radial size). [(c) and (d)] Fourier transform of the peak density, $\hat{n}(\Omega)$, and radial size, $\hat{r}(\Omega)$, calculated as per Eq. (32).

Colleges in Guangdong Province through Grant No. 2019KZDXM001, the Research Fund of Guangdong-Hong Kong-Macao Joint Laboratory for Intelligent Micro-

Nano Optoelectronic Technology through Grant No. 2020B1212030010, and by the Israel Science Foundation through Grant No. 1286/17.

- [1] L. Bergé, Wave collapse in physics: Principles and applications to light and plasma waves, *Phys. Rep.* **303**, 259 (1998).
- [2] C. Sulem and P.-L. Sulem, *The Nonlinear Schrödinger Equation: Self-Focusing and Wave Collapse* (Springer, New York, 1999).
- [3] G. Fibich, *The Nonlinear Schrödinger Equation: Singular Solutions and Optical Collapse* (Springer, Heidelberg, 2015).
- [4] D. Mihalache, D. Mazilu, L. C. Crasovan, I. Towers, B. A. Malomed, A. V. Buryak, L. Torner, and F. Lederer, Stable three-dimensional spinning optical solitons supported by competing quadratic and cubic nonlinearities, *Phys. Rev. E* **66**, 016613 (2002).
- [5] M. Quiroga-Teixeiro and H. Michinel, Stable azimuthal stationary state in quintic nonlinear optical media, *J. Opt. Soc. Am. B* **14**, 2004 (1997).
- [6] K. Dimitrevski, E. Reimhult, E. Svensson, A. Ohgren, D. Anderson, A. Berntson, M. Lisak, and M. L. Quiroga-Teixeiro, Analysis of stable self-trapping of laser beams in cubic-quintic nonlinear media, *Phys. Lett. A* **248**, 369 (1998).
- [7] R. L. Pego and H. A. Warchall, Spectrally stable encapsulated vortices for nonlinear Schrödinger equations, *J. Nonlin. Sci.* **12**, 347 (2002).
- [8] G. Boudebs, S. Cherukulappurath, H. Leblond, J. Troles, F. Smektala, and F. Sanchez, Experimental and theoretical study of higher-order nonlinearities in chalcogenide glasses, *Opt. Commun.* **219**, 427 (2003).
- [9] D. Mihalache, D. Mazilu, L.-C. Crasovan, I. Towers, A. V. Buryak, B. A. Malomed, L. Torner, J. P. Torres, and F. Lederer, Stable Spinning Optical Solitons in Three Dimensions, *Phys. Rev. Lett.* **88**, 073902 (2002).
- [10] H. Michinel, M. J. Paz-Alonso, and V. M. Perez-García, Turning Light into a Liquid Via Atomic Coherence, *Phys. Rev. Lett.* **96**, 023903 (2006).
- [11] E. L. Falcão-Filho, L. Falcão-Filho, C. B. de Araújo, G. Boudebs, H. Leblond, and V. Skarka, Robust Two-Dimensional Spatial Solitons in Liquid Carbon Disulfide, *Phys. Rev. Lett.* **110**, 013901 (2013).
- [12] D. S. Petrov, Quantum Mechanical Stabilization of a Collapsing Bose-Bose Mixture, *Phys. Rev. Lett.* **115**, 155302 (2015).
- [13] D. S. Petrov and G. E. Astrakharchik, Ultradilute Low-Dimensional Liquids, *Phys. Rev. Lett.* **117**, 100401 (2016).
- [14] Y. V. Kartashov, B. A. Malomed, L. Tarruell, and L. Torner, Three-dimensional droplets of swirling superfluids, *Phys. Rev. A* **98**, 013612 (2018).
- [15] H. Sakaguchi, B. Li, and B. A. Malomed, Creation of two-dimensional composite solitons in spin-orbit-coupled self-attractive Bose-Einstein condensates in free space, *Phys. Rev. E* **89**, 032920 (2014).
- [16] L. Salasnich and B. A. Malomed, Localized modes in dense repulsive and attractive Bose-Einstein condensates with spin-orbit and Rabi couplings, *Phys. Rev. A* **87**, 063625 (2013).
- [17] L. Salasnich, W. B. Cardoso, and B. A. Malomed, Localized modes in quasi-two-dimensional Bose-Einstein condensates with spin-orbit and Rabi couplings, *Phys. Rev. A* **90**, 033629 (2014).
- [18] H. Sakaguchi, E. Ya. Sherman, and B. A. Malomed, Vortex solitons in two-dimensional spin-orbit coupled Bose-Einstein condensates: Effects of the Rashba-Dresselhaus coupling and the Zeeman splitting, *Phys. Rev. E* **94**, 032202 (2016).
- [19] Z. Chen, Y. Li, B. A. Malomed, and L. Salasnich, Spontaneous symmetry breaking of fundamental states, vortices, and dipoles in two and one-dimensional linearly coupled traps with cubic self-attraction, *Phys. Rev. A* **96**, 033621 (2017).
- [20] J. S. Aitchison, A. M. Weiner, Y. Silberberg, M. K. Oliver, J. L. Jackel, D. E. Leaird, E. M. Vogel, and P. W. E. Smith, Observation of spatial optical soliton in a nonlinear glass wave-guide, *Opt. Lett.* **15**, 471 (1990).
- [21] Yu. S. Kivshar and D. E. Pelinovsky, Self-focusing and transverse instabilities of solitary waves, *Phys. Rep.* **331**, 117 (2000).
- [22] B. A. Malomed, D. Mihalache, F. Wise, and L. Torner, *J. Opt. B: Quant. Semiclass. Opt.* **7**, R53 (2005); B. A. Malomed, D. Mihalache, F. Wise, and L. Torner, Viewpoint: On multidimensional solitons and their legacy in contemporary atomic, molecular and optical physics, *J. Phys. B: At. Mol. Opt. Phys.* **49**, 170502 (2016).
- [23] G. Assanto, A. A. Minzoni, and N. F. Smyth, Light self-localization in nematic liquid crystals: Modelling solitons in

- nonlocal reorientational media, *J. Nonlin. Opt. Phys. Mater.* **18**, 657 (2009).
- [24] B. A. Malomed, Multidimensional solitons: Well-established results and novel findings, *Eur. Phys. J. Spec. Top.* **225**, 2507 (2016).
- [25] Y. Kartashov, G. Astrakharchik, B. Malomed, and L. Torner, Frontiers in multidimensional self-trapping of nonlinear fields and matter, *Nat. Rev. Phys.* **1**, 185 (2019).
- [26] Z. Luo, W. Pang, B. Liu, Y. Li, and B. A. Malomed, A new form of liquid matter: quantum droplets, *Front. Phys.* **16**, 32201 (2021).
- [27] C. Cabrera, L. Tanzi, J. Sanz, B. Naylor, P. Thomas, P. Cheiney, and L. Tarruell, Quantum liquid droplets in a mixture of Bose-Einstein condensates, *Science* **359**, 301 (2018).
- [28] P. Cheiney, C. R. Cabrera, J. Sanz, B. Naylor, L. Tanzi, and L. Tarruell, Bright Soliton to Quantum Droplet Transition in a Mixture of Bose-Einstein Condensates, *Phys. Rev. Lett.* **120**, 135301 (2018).
- [29] G. Semeghini, G. Ferioli, L. Masi, C. Mazzinghi, L. Wolswijk, F. Minardi, M. Modugno, G. Modugno, M. Inguscio, and M. Fattori, Self-Bound Quantum Droplets of Atomic Mixtures in Free Space, *Phys. Rev. Lett.* **120**, 235301 (2018).
- [30] G. Ferioli, G. Semeghini, L. Masi, G. Giusti, G. Modugno, M. Inguscio, A. Gallelli, A. Recati, and M. Fattori, Collisions of Self-Bound Quantum Droplets, *Phys. Rev. Lett.* **122**, 090401 (2019).
- [31] C. D'Errico, A. Burchianti, M. Prevedelli, L. Salasnich, F. Ancilotto, M. Modugno, F. Minardi, and C. Fort, Observation of quantum droplets in a heteronuclear bosonic mixture, *Phys. Rev. Res.* **1**, 033155 (2019).
- [32] I. Ferrier-Barbut, H. Kadau, M. Wenzel, T. Pfau, Observation of Quantum Droplets in a Strongly Dipolar Bose Gas, *Phys. Rev. Lett.* **116**, 215301 (2016).
- [33] M. Schmitt, M. Wenzel, F. Böttcher, I. Ferrier-Barbut and T. Pfau, Self-bound droplets of a dilute magnetic quantum liquid, *Nature (Lond.)* **539**, 259 (2016).
- [34] I. Ferrier-Barbut, M. Wenzel, F. Böttcher, T. Langen, M. Isoard, S. Stringari and T. Pfau, Scissors Mode of Dipolar Quantum Droplets of Dysprosium Atoms, *Phys. Rev. Lett.* **120**, 160402 (2018).
- [35] L. Chomaz, S. Baier, D. Petter, M. J. Mark, F. Wachtler, L. Santos, and F. Ferlaino, Quantum-Fluctuation-Driven Crossover from a Dilute Bose-Einstein Condensate to a Macrodroplet in a Dipolar Quantum Fluid, *Phys. Rev. X* **6**, 041039 (2016).
- [36] F. Dalfovo and S. Stringari, Bosons in anisotropic traps: Ground state and vortices, *Phys. Rev. A* **53**, 2477 (1996).
- [37] S. K. Adhikari, Collapse of attractive Bose-Einstein condensed vortex states in a cylindrical trap, *Phys. Rev. E* **65**, 016703 (2001).
- [38] T. J. Alexander and L. Bergé, Ground states and vortices of matter-wave condensates and optical guided waves, *Phys. Rev. E* **65**, 026611 (2002).
- [39] H. Saito and M. Ueda, Split Instability of a Vortex in an Attractive Bose-Einstein Condensate, *Phys. Rev. Lett.* **89**, 190402 (2002).
- [40] H. Saito and M. Ueda, Split-merge cycle, fragmented collapse, and vortex disintegration in rotating Bose-Einstein condensates with attractive interactions, *Phys. Rev. A* **69**, 013604 (2004).
- [41] D. Mihalache, D. Mazilu, B. A. Malomed, and F. Lederer, Vortex stability in nearly-two-dimensional Bose-Einstein condensates with attraction, *Phys. Rev. A* **73**, 043615 (2006).
- [42] L. D. Carr and C. W. Clark, Vortices in Attractive Bose-Einstein Condensates in Two Dimensions, *Phys. Rev. Lett.* **97**, 010403 (2006).
- [43] B. A. Malomed, F. Lederer, D. Mazilu, and D. Mihalache, On Stability of Vortices in Three-Dimensional Self-Attractive Bose-Einstein Condensates, *Phys. Lett. A* **361**, 336 (2007).
- [44] L. D. Carr and Y. Castin, Dynamics of a matter-wave bright soliton in an expulsive potential, *Phys. Rev. A* **66**, 063602 (2002).
- [45] L. Salasnich, Dynamics of a Bose-Einstein-condensate bright soliton in an expulsive potential, *Phys. Rev. A* **70**, 053617 (2004).
- [46] Z. X. Liang, Z. D. Zhang, and W. M. Liu, Dynamics of a Bright Soliton in Bose-Einstein Condensates with Time-Dependent Atomic Scattering Length in an Expulsive Parabolic Potential, *Phys. Rev. Lett.* **94**, 050402 (2005).
- [47] W. B. Cardoso, A. T. Avelar, and D. Bazeia, Bright and dark solitons in a periodically attractive and expulsive potential with nonlinearities modulated in space and time, *Nonlin. Anal.: Real World Appl.* **11**, 4269 (2010).
- [48] S. Rajendran, P. Muruganandam, and M. Lakshmanan, Bright and dark solitons in a quasi-1D Bose-Einstein condensates modelled by 1D Gross-Pitaevskii equation with time-dependent parameters, *Physica D* **239**, 366 (2010).
- [49] N. H. Xuan and M. Zuo, Matter-wave solitons in two-component Bose-Einstein condensates with tunable interactions and time varying potential, *Commun. Theor. Phys.* **56**, 1035 (2011).
- [50] S. Rajendran, M. Lakshmanan, and P. Muruganandam, Matter wave switching in Bose-Einstein condensates via intensity redistribution soliton interactions, *J. Math. Phys.* **52**, 023515 (2011).
- [51] A. D. Campo and M. G. Boshier, Shortcuts to adiabaticity in a time-dependent box, *Sci. Rep.* **2**, 648 (2012).
- [52] R. Radha, P. S. Vinayagam, J. B. Sudharsan, and B. A. Malomed, Persistent bright solitons in sign-indefinite coupled nonlinear Schrödinger equations with a time-dependent harmonic trap, *Commun. Nonlin. Sci. Numer. Simul.* **31**, 30 (2016).
- [53] Y. V. Kartashov and V. V. Konotop, Stable Nonlinear Modes Sustained by Gauge Fields, *Phys. Rev. Lett.* **125**, 054101 (2020).
- [54] B. V. Gisin and A. A. Hardy, Stationary solutions of plane nonlinear-optical antiwaveguides, *Opt. Quant. Electron.* **27**, 565 (1995).
- [55] B. V. Gisin, A. Kaplan, and B. A. Malomed, Spontaneous symmetry breaking and switching in planar nonlinear optical antiwaveguides, *Phys. Rev. E* **62**, 2804 (2000).
- [56] D. Bortman-Arbiv, A. D. Wilson-Gordon, and H. Friedmann, Strong parametric amplification by spatial soliton-induced cloning of transverse beam profiles in an all-optical antiwaveguide, *Phys. Rev. A* **63**, 031801(R) (2001).
- [57] O. N. Verma and T. N. Dey, Steering, splitting, and cloning of an optical beam in a coherently driven Raman gain system, *Phys. Rev. A* **91**, 013820 (2015).

- [58] A. Kaplan, B. V. Gisin, and B. A. Malomed, Stable propagation and all-optical switching in planar waveguide-antiwaveguide periodic structures, *J. Opt. Soc. Am. B* **19**, 522 (2002).
- [59] X. Chen, A. Ruschhaupt, S. Schmidt, A. del Campo, D. Guery-Odelin, and J. G. Muga, Fast Optimal Frictionless Atom Cooling in Harmonic Traps: Shortcut to Adiabaticity, *Phys. Rev. Lett.* **104**, 063002.
- [60] D. Stefanatos, J. Ruths, and J. S. Li, Frictionless atom cooling in harmonic traps: A time-optimal approach, *Phys. Rev. A* **82**, 063422 (2010).
- [61] R. Grimm, M. Weidemüller, and Y. B. Ovchinnikov, Optical dipole traps for neutral atoms, *Adv. At. Mol. Opt. Phys.* **42**, 95 (2000).
- [62] P. W. Courteille, V. S. Bagnato, and V. I. Yukalov, Bose-Einstein condensation of trapped atomic gases, *Laser Phys.* **11**, 659 (2001).
- [63] B. A. Malomed, *Soliton Management in Periodic Systems* (Springer, New York, 2006).
- [64] S. K. Turitsyn, B. G. Bale, and M. P. Fedoruk, Dispersion-managed solitons in fibre systems and lasers, *Phys. Rep.* **521**, 135 (2012).
- [65] I. Towers and B. A. Malomed, Stable (2+1)-dimensional solitons in a layered medium with sign-alternating Kerr nonlinearity, *J. Opt. Soc. Am. B* **19**, 537 (2002).
- [66] F. Kh. Abdullaev, J. G. Caputo, R. A. Kraenkel, and B. A. Malomed, Controlling collapse in Bose-Einstein condensation by temporal modulation of the scattering length, *Phys. Rev. A* **67**, 013605 (2003).
- [67] H. Saito and M. Ueda, Dynamically Stabilized Bright Solitons in a Two-Dimensional Bose-Einstein Condensate, *Phys. Rev. Lett.* **90**, 040403 (2003).
- [68] A. Itin, T. Morishita, and S. Watanabe, Reexamination of dynamical stabilization of matter-wave solitons, *Phys. Rev. A* **74**, 033613 (2006).
- [69] L. P. Pitaevskii and S. Stringari, *Bose-Einstein Condensation* (Oxford University Press, Oxford, 2003).
- [70] R. Y. Chiao, E. Garmire, and C. H. Townes, Self-Trapping of Optical Beams, *Phys. Rev. Lett.* **13**, 479 (1964).
- [71] L. Chierchia and G. Gallavotti, Drift and diffusion in phase space, *Ann. Inst. H. Poincaré Phys. Théor.* **60**, 1 (1994).
- [72] K. W. Mahmud, H. Perry, and W. P. Reinhardt, Quantum phase-space picture of Bose-Einstein condensates in a double well, *Phys. Rev. A* **71**, 023615 (2005).
- [73] G. D. Montesinos, V. M. Pérez-García, H. Michinel, and J. R. Salgueiro, Stabilized vortices in layered Kerr media, *Phys. Rev. E* **71**, 036624 (2005).
- [74] M. Desaix, D. Anderson, and M. Lisak, Variational approach to collapse of optical pulses, *J. Opt. Soc. Am. B* **8**, 2082 (1991).
- [75] F. Kh Abdullaev and R. Galimzyanov, The dynamics of bright matter wave solitons in a quasi one-dimensional Bose-Einstein condensate with a rapidly varying trap, *J. Phys. B: At. Mol. Opt. Phys.* **36**, 1099 (2003).
- [76] F. Arscott, *Periodic Differential Equations: An Introduction to Mathieu, Lamé and Allied Functions* (Pergamon Press, New York, 1964).
- [77] L. D. Landau and E. M. Lifshitz, *Mechanics* (Nauka, Moscow, 1988).
- [78] M. Wickramasinghe and J. M. Berg, Vibrational control of Mathieu's equation, in *Proceedings of the IEEE/ASME International Conference on Advanced Intelligent Mechatronics (AIM'13)* (Wollongong, Australia, 2013).
- [79] V. P. Ermakov, Second-order differential equations: Conditions of complete integrability, *Univ. Izv. Kiev Ser. III* **9**, 1 (1880); P. Ermakov Vasilij, Second-order differential equations: Conditions of complete integrability, *English translation, Applic. Anal. Discr. Math.* **2**, 123 (2008).
- [80] P. G. L. Leach and S. K. Andriopoulos, The Ermakov equation: A commentary, *Applic. Anal. Discr. Math.* **2**, 146 (2008).
- [81] E. Pinney, The nonlinear differential equation $y'' + p(x)y + c/y^3 = 0$, *Proc. Am. Math. Soc.* **1**, 681 (1950).
- [82] H. R. Lewis, Jr., Classical and Quantum Systems with Time-Dependent Harmonic-Oscillator-Type Hamiltonians, *Phys. Rev. Lett.* **18**, 510 (1967).
- [83] H. R. Lewis Jr., Class of exact invariants for classical and quantum time-dependent harmonic oscillators, *J. Math. Phys.* **9**, 1976 (1968).
- [84] M. A. Lohe, Exact time dependence of solutions to the time-dependent Schrödinger equation, *J. Phys. A: Math. Theor.* **42**, 035307 (2009).
- [85] M. L. Chiofalo, S. Succi, and M. P. Tosi, Ground state of trapped interacting Bose-Einstein condensates by an explicit imaginary-time algorithm, *Phys. Rev. E* **62**, 7438 (2000).
- [86] W. Bao and Q. Du, Computing the ground state solution of Bose-Einstein condensates by a normalized gradient flow, *SIAM J. Sci. Comput.* **25**, 1674 (2004).
- [87] J. Yang, *Nonlinear Waves in Integrable and Nonintegrable Systems* (SIAM, Philadelphia, 2010).
- [88] F. K. Abdullaev and M. Salerno, Gap-Townes solitons and localized excitations in low-dimensional Bose-Einstein condensates in optical lattices, *Phys. Rev. A* **72**, 033617 (2005).
- [89] K. Senthilnathan, Q. Li, K. Nakkeeran, and P. K. A. Wai, Robust pedestal-free pulse compression in cubic-quintic nonlinear media, *Phys. Rev. A* **78**, 033835 (2008).
- [90] E. Shamriz, Z. Chen, and B. A. Malomed, Stabilization of one-dimensional Townes solitons by spin-orbit coupling in a dual-core system, *Commun. Nonlin. Sci. Numer. Simul.* **91**, 105412 (2020).
- [91] A. L. Fetter, Rotating vortex lattice in a Bose-Einstein condensate trapped in combined quadratic and quartic radial potentials, *Phys. Rev. A* **64**, 063608 (2001).
- [92] K. Kasamatsu, M. Tsubota, and M. Ueda, Giant hole and circular superflow in a fast rotating Bose-Einstein condensate, *Phys. Rev. A* **66**, 053606 (2002).
- [93] V. Bretin, S. Stock, Y. Seurin, and J. Dalibard, Fast Rotation of a Bose-Einstein Condensate, *Phys. Rev. Lett.* **92**, 050403 (2004).
- [94] A. D. Jackson, G. M. Kavoulakis, and E. Lundh, Phase diagram of a rotating Bose-Einstein condensate with anharmonic confinement, *Phys. Rev. A* **69**, 053619 (2004).